

Multiwavelength Monitoring of the Dwarf Seyfert 1 Galaxy NGC 4395. II. X-ray and Ultraviolet Continuum Variability

Paul M. O’Neill¹, Shai Kaspi^{2,3}, Ari Laor², Kirpal Nandra¹, Edward C. Moran⁴, Bradley M. Peterson⁵, Louis-Benoit Desroches⁶, Alexei V. Filippenko⁶, Luis C. Ho⁷, and Dan Maoz³

ABSTRACT

We report on two *Chandra* observations, and a simultaneous *Hubble Space Telescope* ultraviolet observation, of the dwarf Seyfert 1 galaxy NGC 4395. Each *Chandra* observation had a duration of ~ 30 ks, with a separation of ~ 50 ks. The spectrum was observed to harden between these observations via a scaling down of the soft-band flux. The inter-observation variability is in a different sense to the observed variability within each observation and is most likely the result of increased absorption. Spectral variations were seen during the first observation suggesting that the X-ray emission is produced in more than one disconnected region. We have also re-analyzed a ~ 17 ks *Chandra* observation conducted in 2000. During the three *Chandra* observations the 2–10 keV flux is about a factor of 2 lower than seen during an *XMM-Newton* observation conducted in 2003. Moreover, the fractional variability amplitude exhibited during the *XMM-Newton* observation is significantly softer than seen during the *Chandra* observations. A power-spectral analysis of the first of the two new *Chandra* observations revealed a peak at 341 s with a formal detection significance of 99 %. A similar peak was seen previously in the 2000 *Chandra* data. However, the detection of this feature is tentative given that it was found in neither the second of our two new *Chandra* observations nor the *XMM-Newton* data, and it is much narrower than expected. The *Hubble Space Telescope* observation was conducted during part of the second

¹Astrophysics Group, Imperial College London, Blackett Laboratory, Prince Consort Road, London SW7 2AZ, United Kingdom; p.oneill@imperial.ac.uk

²Department of Physics, Technion, Haifa 32000, Israel

³Wise Observatory and School of Physics and Astronomy, Tel-Aviv University, Tel-Aviv 69978, Israel

⁴Astronomy Department, Wesleyan University, Van Vleck Observatory, Middletown, CT 06459

⁵Department of Astronomy, Ohio State University, 140 West 18th Avenue, Columbus, OH 43210

⁶Department of Astronomy, University of California, Berkeley, CA 94720-3411

⁷Carnegie Observatories, 813 Santa Barbara Street, Pasadena, CA 91101

Chandra visit. A zero-lag correlation between the ultraviolet and X-ray fluxes was detected with a significance of $\sim 99.5\%$, consistent with the predictions of the two-phase model for the X-ray emission from active galactic nuclei.

Subject headings: galaxies: active—galaxies: individual (NGC 4395)—galaxies: Seyfert—ultraviolet: galaxies—X-rays: galaxies

1. INTRODUCTION

The Sd galaxy NGC 4395 harbors a Seyfert 1 nucleus having the lowest-known luminosity and black hole mass for any object of its class (Filippenko & Sargent 1989; Filippenko, Ho, & Sargent 1993; Filippenko & Ho 2003). A recent reverberation mapping campaign yielded a black hole mass of $M_{\bullet} = (3.6 \pm 0.6) \times 10^5 M_{\odot}$ and a luminosity corresponding to 0.1 % of the Eddington limit (Peterson et al. 2005). NGC 4395 thus offers the opportunity to study active galactic nuclei (AGNs) at the low end of the mass scale. This is particularly useful in the context of unifying our understanding of the X-ray emission from AGNs and galactic black hole binaries.

NGC 4395 exhibits strong and rapid X-ray variability. The best data in this regard are from a recent *XMM-Newton* observation, which provided an almost uninterrupted light curve of ~ 90 ks duration. The power spectrum of the 0.2–10 keV variability could be modeled with a singly broken power law, with a break timescale of ~ 500 s (Vaughan et al. 2004). Moreover, the amplitude of the variations was found to decrease with increasing energy. X-ray spectral variability in NGC 4395 had been studied previously using both *ASCA* and *Chandra* data. The *ASCA* data were modeled with a multi-zone warm absorber, and the spectral variability was suggestive of flux-correlated variations in the ionization parameter of one of these absorbers (Iwasawa et al. 2000; Shih et al. 2003). In the *Chandra* data, spectral variations were seen on a timescale of several hundred seconds and these were interpreted to be the result of column density fluctuations (Moran et al. 2005). Contrary to the *ASCA* observations, the *Chandra* data exhibited only a marginally significant variation in spectral shape with overall flux. Moran et al. (2005) also reported the presence of a transient ~ 400 s modulation in the *Chandra* data, with a detection significance of $\gtrsim 95\%$

Simultaneous X-ray and ultraviolet (UV) observations are very valuable in the study of AGNs. In the two-phase model for the production of the X-ray emission, seed photons from an optically thick accretion disk are inverse-Compton scattered by hot electrons in the disk corona (e.g., Sunyaev & Titarchuk 1980; Haardt & Maraschi 1993). A portion of the X-ray flux is directed down toward the disk to be thermally reprocessed into seed photons

(Guilbert & Rees 1988). Given that the two phases (i.e. disk and corona) are so closely coupled, simultaneous UV and X-ray data can yield information regarding the disk–corona system (e.g., Nandra et al. 2000; Petrucci et al. 2004).

In this paper, we present a variability analysis of two ~ 30 ks *Chandra* observations that were obtained as part of a multiwavelength monitoring campaign on NGC 4395. The results from the UV line variability analysis from this campaign are presented in Peterson et al. (2005), and the optical results are described by Desroches et al. (2006). We have also re-analyzed the previous ~ 17 ks *Chandra* observation from 2000 and, for the purpose of a comparison with the *Chandra* data, we have re-analyzed the ~ 90 ks *XMM-Newton* observation. Finally, we have investigated the X-ray–UV relationship using the simultaneous data obtained during the second *Chandra* observation.

2. OBSERVATIONS AND DATA REDUCTION

Chandra observed NGC 4395 on 2004 April 10, from 02:43 to 11:39 UT, and on April 11, from 01:05 to 10:11 UT. We hereafter refer to the first and second observations as “visit 1” and “visit 2,” respectively. The observations were conducted using the S3 chip of the ACIS-S instrument. A 1/8 subarray was selected, with each 0.44104 s frame having an actual exposure time of 0.4 s (i.e., live-time ~ 91 %). The *Chandra* observation presented by Moran et al. (2005, see § 1) was conducted on 2000 June 20, from 03:04 to 07:56 UT, and we shall refer to it by its observation identification number 882. A 1/2 subarray was selected for observation 882, which yielded frame and exposure times of 1.54104 s and 1.5 s, respectively (i.e. live-time ~ 97 %). Level 2 events files were created in the standard manner using CIAO 3.2.1 and CALDB 3.0.1. All observations were uninterrupted and no background flares were present. The total good exposure times were ~ 27 ks, ~ 28 ks, and ~ 17 ks for visit 1, visit 2, and observation 882, respectively. Moran et al. (2005) showed that photon pile-up does not significantly affect observation 882, and the shorter frame time used for visits 1 and 2 ensures that pile-up is not a problem for those observations either.

Source events were extracted from within a circular aperture, centered on the source, with a radius of 10 pixels ($\sim 5''$). The background was estimated from an annulus surrounding the source region, with inner and outer radii of 20 and 55 pixels, respectively. Light curves were then extracted from these events files, with the time resolution chosen to be an integer multiple of the frame time. For visit 1 and visit 2, we used time bins of 299.9072 s, 599.8144 s, and 999.83768 s, respectively, for the “300 s,” “600 s,” and “1000 s” light curves. For observation 882, we used time bins of 300.5028 s, 601.0056 s, and 1000.13496 s. The data were resolved into three (0.4–2.7, 2.7–4.2, 4.2–8.0 keV) and also two (0.4–3.4, 3.4–8.0 keV)

energy ranges. The boundaries of these energy ranges were selected so that each band has roughly the same signal-to-noise ratio. We shall refer to the 0.4–8.0 keV, 0.4–3.4 keV, and 3.4–8.0 keV energy ranges as the “full,” “soft,” and “hard” bands, respectively. Furthermore, we define “softness” to be the ratio between the counting rates in these soft and hard bands. Resolving the data into three energy bands, with a time bin of 600 s, yields an average of roughly 20 counts bin^{-1} .

As well as binning the events in equal time intervals, we constructed light curves with a variable bin width. The start time of each bin was defined to be the midpoint in time between two consecutive photon arrival times. The length of each time bin was then set such that each bin contained exactly 30 counts. The stop time of the bin was defined to be the midpoint in time between the last count in that bin and the next event. Smoothing was achieved by using overlapping bins, such that adjacent bins in the smoothed light curves share a common set of 29 counts.

Various light curves for visit 1, visit 2, and observation 882 are presented in Figs. 1, 2, and 3, respectively. The top panel in each of these figures shows the full-band (0.4–8.0 keV), 300 s light curve. Smoothed light curves, resolved into three energy bands, are shown in the second panel. In the third panel we show 600 s soft-band and hard-band light curves. Finally, the softness ratio using a 600 s time resolution is given in the lowest panel. In this panel in Fig. 1, we have overlaid 7 points from the softness time series using 1000 s bins. The meaning of these points is explained in § 3.2. The error bars are 1σ , and the time origins are MJD 53105.12824, MJD 53106.06050, and MJD 51715.13164 for visit 1, visit 2, and observation 882, respectively.

The visit 1 and visit 2 *Chandra* observations were carried out simultaneously with *HST* Space Telescope Imaging Spectrograph (STIS) observations, which are described by Peterson et al. (2005). The *HST* observation during visit 1 was acquired under gyro control, which degraded the photometric accuracy and rendered this observation unusable. Therefore, our X-ray–UV correlation analysis uses only the visit 2 data. Note that, owing to a data processing error, the fluxes given by Peterson et al. (2005) are too high by a factor of 7.96. The UV fluxes presented here have been scaled to the correct values.

We have also performed an analysis of the archived *XMM-Newton* data on NGC 4395 to facilitate a comparison with the *Chandra* data. This observation was conducted on 2003 November 30 and December 1 for ~ 110 ks. We used only the earliest 90 ks of the observation, during which the background was low and stable. A variability analysis of these data was presented by Vaughan et al. (2004).

3. X-RAY VARIABILITY

3.1. Normalized Excess Variance

One method of investigating spectral variability is to compute the excess variance in the light curve as a function of energy. We sub-divided the visit 1 and visit 2 light curves (600 s time resolution) each into 2 halves, thus creating four light curve segments having roughly the same duration as the entire light curve from observation 882. We resolved these light curves into various energy bands and measured the normalized excess variance (i.e., excess variance divided by the mean-squared; see, e.g., Vaughan et al. 2003a).

The uncertainties were calculated directly from the data via Monte Carlo simulations. For each light curve, we performed 1000 simulations in which we added Poisson noise to the observed light curve and calculated the normalized excess variance. The standard deviation of the 1000 simulated values of normalized excess variance was then taken to be the uncertainty owing *only* to Poisson noise. For each energy band, we determined the mean of each pair of measurements from visit 1 and visit 2, and the uncertainties were propagated.

The values of normalized excess variance for visit 1, visit 2, and observation 882 are listed in Table 1, where we also give the mean variance obtained from all 5 *Chandra* light curve segments. The ratios between the excess variances in the 0.4–2.7 keV and 4.2–8.0 keV bands are 1.5 ± 0.6 , 1.5 ± 0.7 , and 2.4 ± 0.9 for visit 1, visit 2, and observation 882, respectively. These ratios are all consistent with unity, and are thus consistent with there being no spectral variability during each of these observations. Considering all of the *Chandra* light curves combined, the ratio between the excess variances in the 2.7–4.2 keV and 4.2–8.0 keV bands is 1.4 ± 0.3 , which is also clearly consistent with unity. However, the ratio between the 0.4–2.7 keV and 4.2–8.0 keV bands is 1.7 ± 0.4 , providing marginal ($\sim 2\sigma$) evidence for the presence of enhanced soft variability. Note also that there *is* evidence for enhanced soft variability during observation 882: the *difference* between the 0.4–2.7 keV and 4.2–8.0 keV variances is $(13 \pm 5) \times 10^{-2}$, which is significant at the $\sim 2.5\sigma$ level.

We also wished to compare the *Chandra* observations with the *XMM-Newton* observation. We subdivided the *XMM-Newton* light curve into 6 segments, each with a duration of ~ 15 ks, and selected the same energy bands that we used for the *Chandra* data. The mean excess variances from the *XMM-Newton* data are listed in Table 1, and the variances from both the *Chandra* and *XMM-Newton* observations are plotted in Fig. 4. The ratio between the variances in the 2.7–4.2 keV and 4.2–8.0 keV bands is 1.6 ± 0.2 , which is consistent with that seen during the three *Chandra* observations. Considering instead the 0.4–2.7 keV and 4.2–8.0 keV bands, the ratio between the excess variances is 5.2 ± 0.4 . The variability is thus clearly softer during the *XMM-Newton* observation compared to the *Chandra* observations.

3.2. Correlation Analysis

As well as examining the relative magnitudes of the variations in different energy bands, we have also investigated the correlations that exist between them. This is useful because the excess-variance analysis is not sensitive to the presence of phase differences between the variations in the different energy bands.

The “softness” was defined to be the counting rate ratio between the 0.4–3.4 keV and 3.4–8.0 keV bands (see Figs. 1–3). During visit 2 and observation 882, using a time resolution of both 600 s and 1000 s, the softness is consistent with being constant. During visit 1, however, the softness is variable with a significance of 97 % and 99 %, respectively, when using time resolutions of 600 s and 1000 s.

In Fig. 5 we show the relationship between the 0.4–3.4 keV and 3.4–8.0 keV intensities for all three observations, using a time resolution of 1000 s. We performed a chi-squared straight-line fit for each observation, taking into account the uncertainties in both coordinates (Press et al. 2001). These fits were satisfactory for visit 2 and observation 882. The fit for visit 1, however, was poor ($\chi^2/\text{DOF} = 45.0/27$), revealing the presence of scatter about the mean relation, with a significance of 98.4 %. The mean relations in Fig. 5 are all consistent with passing through the origin, so there is no significant softening of the spectrum with increasing flux.

In Fig. 5, there are seven points during visit 1 that deviate from the straight line such that they contribute $\Delta\chi^2 > 2$ to the total χ^2 . These points are plotted as open circles in the bottom panel of Fig. 1. These deviations can be investigated further by resolving the data into narrower energy bands. We thus defined hard color to be the ratio between the 2.7–4.2 keV and 4.2–8.0 keV intensities, while soft color is the ratio between the 0.4–2.7 keV and 4.2–8.0 keV intensities. We performed chi-squared tests and found that both the hard and soft colors are consistent with being constant over the duration of visit 1, and the relationship between these colors is consistent with Poisson noise. The low signal-to-noise ratio of the data thus limits our ability to examine the spectral deviations in detail.

Between visit 1 and visit 2 the gradient of the linear relation between the 0.4–2.7 keV and 4.2–8.0 keV counting rates (1000 s time resolution) exhibits a significant decrease, from 1.62 ± 0.23 during visit 1 to 0.87 ± 0.15 during visit 2. Between these observations, then, the soft-band intensity has been scaled down relative to that in the hard band. Note also that, in Fig. 5, the “track” for observation 882 extends to higher values of hard and soft intensity compared to the other two observations.

Cross-correlation functions (CCFs) were calculated for each of the *Chandra* observations using a time resolution of 600 s. We used the methods described in § 4 and the analysis was

performed on two pairs of energy bands: 0.4–3.4 keV and 3.4–8.0 keV, and 0.4–2.7 keV and 4.2–8.0 keV. No significant lags were found, nor did we find any clear asymmetries in the CCFs. The 95 % upper limits on the time lags were roughly ± 1 hour.

3.3. Power-Spectral Analysis

A previous analysis of observation 882 revealed some evidence for the presence of quasi-periodic oscillations with a period of ~ 400 s (Moran et al. 2005). We decided, therefore, to search the visit 1 and visit 2 data for possible periodicities. We generated power spectra from the 0.4–8.0 keV light curves with a time resolution of 10.14392 s (corresponding to 23 frames). The frequency step was 3.36×10^{-5} Hz in the visit 1 power spectrum and 3.21×10^{-5} Hz for visit 2. The base-10 logarithms of power and frequency were calculated, and we added 0.25068 to each of the logarithmic powers to remove the bias that is associated with this transformation (Papadakis & Lawrence 1993; Vaughan 2005). A plot of the logarithm of power (fractional-rms-squared per Hz) versus logarithm of frequency from visit 1 is shown in Fig 6.

We followed the prescription of Vaughan (2005) to search for possible periodicities. For visit 1, the power spectrum was divided into two frequency ranges, above and below $10^{-2.8}$ Hz (the Poisson noise appears to dominate the power spectrum at frequencies higher than this), so that the power-law continuum could be modeled adequately in logarithm-logarithm space using a linear function. The lower-frequency part of the visit 1 power spectrum had a slope of -0.8 ± 0.2 , and the higher-frequency part was consistent with white noise. The power was calculated at a total of 1464 frequencies over the entire frequency range so we adopted this as the “number-of-trials.” The most significant peak in visit 1 was found at a frequency of 2.93×10^{-3} Hz, corresponding to a period of 341 s, with a significance of 99.0 % (see Fig. 6). There is no evidence for any signal power in the adjacent frequency bins, so any periodicity, if actually present, would probably have a quality factor ($Q = \nu/FWHM$) of greater than ~ 90 . The detection significance of the peak might depend somewhat on the frequency at which the spectrum is divided into two halves. Assuming the division to be located at $10^{-2.5}$ Hz and $10^{-2.45}$ Hz (i.e., the peak is on top of the flicker noise component) yielded significance levels of 99.3 % and 98.5 %, respectively. We also examined visit 2 and the *XMM-Newton* data in a similar fashion to visit 1 and found no evidence for a periodicity.

We also re-analyzed observation 882 to compare the methods we have used here with the analysis of Moran et al. (2005). A power spectrum was generated from the 0.4–8.0 keV light curve, with a time resolution of 9.24624 s (corresponding to 6 frames). In this power spectrum, the boundary between the upper- and lower-frequency halves was chosen to be

$10^{-2.4}$ Hz. The most significant peak was at a frequency of 2.50×10^{-3} Hz, corresponding to a period of 400 s, with a significance of 28 %. Then, following the analysis of Moran et al. (2005), we generated a power spectrum using a light curve from only the second half of the observation. The significance of the peak in this case was 95.0 %, in agreement with Moran et al. (2005), and the frequency of the peak corresponds to a period of 390 s. (Note that Moran et al. (2005) interpolated between Fourier frequencies and located the peak at 396 s.)

4. X-RAY–UV CORRELATION

4.1. Cross-Correlation Analysis

The *HST/STIS* light curve at 1350 Å, with a time resolution of 200 s, is shown in Fig. 7 (top). We have cross-correlated this light curve with the 0.4–8.0 keV light curve binned to 300 s, shown in Fig. 7 (bottom). We used two cross-correlation methods, one being the interpolated cross-correlation function (ICCF; e.g., Gaskell & Sparke 1986; White & Peterson 1994; Peterson et al. 2004), and the other being the z-transform discrete correlation function (ZDCF) of Alexander (1997), which is an improvement of the discrete correlation Function (DCF; Edelson & Krolik 1988). The results of the cross-correlations are plotted in Fig. 8, in which we show lags that are symmetrical about zero and for which there are at least 20 lags for each bin in the ZDCF. The two different methods are in very good agreement for these data.

To calculate the uncertainties in the cross-correlation lag determination we used the model-independent FR/RSS Monte Carlo method of Peterson et al. (2005, 1998). In this method, each Monte Carlo simulation is composed of two parts. The first is a “random subset selection” (RSS) procedure which consists of randomly drawing, with replacement, from a light curve of N points a new sample of N points. After the N points are selected, the redundant selections are removed from the sample such that the temporal order of the remaining points is preserved. This procedure reduces the number of points in each light curve by a factor of $\sim 1/e$ and accounts for the effect that individual data points have on the cross-correlation. The second part is “flux randomization” (FR), in which the observed fluxes are altered by random Gaussian deviates scaled to the uncertainty ascribed to each point. This procedure simulates the effect of measurement uncertainties. The two resampled and altered time series are cross-correlated using the ICCF method and the centroid of the CCF is computed. We used ~ 1000 Monte Carlo realizations to build up a cross-correlation centroid distribution (CCCD; Maoz & Netzer 1989). The mean of the distribution is taken to be the time lag and the uncertainty is determined as the range that contains 68 % of the Monte Carlo realizations in the CCCD and thus would correspond to 1σ uncertainties for

a normal distribution. We find the time lag between the UV and X-ray light curves to be -300 ± 1400 s, which is clearly consistent with zero time lag, with a 95 % upper limit of roughly ± 1 hour.

4.2. Light-Curve Simulations

While the X-ray–UV correlation appears to be significant, an apparently strong correlation could be the result of a chance alignment of two uncorrelated “flicker-noise” or “red-noise” light curves. If the power spectrum of a light curve exhibits either flicker-noise or red-noise, then a correlation will exist between points that are nearby in time. Consequently, the *effective* number of independent points in each light curve is less than the actual number of points. Therefore, in the case that the two light curves are uncorrelated, the probability of exceeding a certain correlation coefficient is greater than in the case of comparing two light curves that originate from a “white-noise” process.

To test whether we have observed a significant correlation, we simulated X-ray light curves and cross-correlated them against the observed UV light curve. The power spectrum of the visit 2 0.4–8.0 keV light curve (see Fig. 7 bottom) had a power-law index of $\alpha = 0.86 \pm 0.12$, and we used this value for the underlying mean power spectrum. We initially used the method of Timmer & Konig (1995) to simulate linear light curves. However, it was not possible to reproduce the observed fractional variance unless negative counting rates were permitted. Therefore, following Uttley et al. (2005), we performed an exponential transformation on the linear light curves. We were thus able to simulate light curves having the required power-law index and variance, while also maintaining positive counting rates. As shown by Uttley et al. (2005), the exponential transformation slightly alters the slope of the power spectrum. We adopted a method of trial-and-error to generate power spectra having the required mean power-law index. Note also that an exponential transform is more appropriate than using a linear model because the transformed light curves contain the so-called “rms-flux” correlation, which has been observed in NGC 4395 (Vaughan et al. 2004).

For each synthesized X-ray light curve we calculated the ZDCF and found the largest correlation coefficient in the range of lags shown in Fig. 8. We found that only 50 of the 10000 simulations had a coefficient larger than that observed, which corresponds to a detection significance of 99.5 %. It is possible that the true, underlying power spectrum has a steeper index than the best-fitting value of 0.86, so this significance level may be overestimated. If we adopt instead a value of 1.10, which is 2σ higher than the best-fitting value, then the significance is reduced to 99.4 %. Alternatively, the significance is increased to 99.8 % if we

use a flatter slope of $\alpha = 0.65$.

4.3. Simultaneous UV–X-ray Observations

We also examined the X-ray and UV data that were collected exactly simultaneously. The correlation between the X-ray and UV fluxes, using a time resolution of 400 s, is shown in Fig. 9. As shown by the line in Fig. 9, the UV flux, relative to the X-ray intensity, has a constant component of $\sim 7 \times 10^{-16} \text{ erg cm}^{-2} \text{ s}^{-1} \text{ \AA}^{-1}$. The presence of this constant component is noticeable also when comparing the variability of the X-ray and UV light curves. The normalized excess variances of the simultaneous 0.4–8.0 keV and UV data shown in Fig. 9 are $(23 \pm 4) \times 10^{-2}$ and $(2.0 \pm 0.3) \times 10^{-2}$, respectively. Over the same range in timescales the X-ray variability, *when normalized by the mean*, is thus clearly stronger than the UV variability.

It is useful to compare directly the fluxes in the *variable* components of the simultaneous X-ray and UV data because the variable UV emission is possibly the result of X-ray reprocessing. The square-root of the *unnormalized* excess variance (i.e., the “excess rms”) in the UV data is $(1.5 \pm 0.1) \times 10^{-16} \text{ erg cm}^{-2} \text{ s}^{-1} \text{ \AA}^{-1}$. This corresponds to a monochromatic flux variability at 1350 Å of $2.0 \times 10^{-13} \text{ erg cm}^{-2} \text{ s}^{-1}$. In the X-ray data, the unnormalized excess variance is $(4.7 \pm 0.4) \times 10^{-2} \text{ counts s}^{-1}$. To convert this counting rate into a flux, we modeled the visit 2 X-ray spectrum over the range 1.3–8.0 keV using a power law modified by neutral absorption. The flux at 1 keV of the underlying power-law was $5.0 \times 10^{-13} \text{ erg cm}^{-2} \text{ s}^{-1} \text{ keV}^{-1}$. The observed variability in the counting rate then corresponds to a monochromatic variability at 1 keV of $2.4 \times 10^{-13} \text{ erg cm}^{-2} \text{ s}^{-1}$, very similar to that of the UV.

Finally, we note that the mean monochromatic flux at 1350 Å is $1.4 \times 10^{-12} \text{ erg cm}^{-2} \text{ s}^{-1}$. This is a factor of ~ 3 greater than the mean monochromatic flux at 1 keV. The monochromatic flux of the constant UV component is $9.3 \times 10^{-13} \text{ erg cm}^{-2} \text{ s}^{-1}$.

5. DISCUSSION

5.1. Summary of Results

We have analyzed three *Chandra* observations of the dwarf Seyfert 1 NGC 4395. The first two observations, visit 1 and visit 2, each have a duration of ~ 30 ks and are separated by ~ 50 ks (end of visit 1 to beginning of visit 2), and were obtained as part of a multiwavelength

monitoring campaign. The third observation was obtained 4 years earlier and has a duration of ~ 17 ks. We have also analyzed the ~ 90 ks *XMM-Newton* observation from 2003 to facilitate a comparison with the *Chandra* data.

The normalized excess variances on timescales $\lesssim 15$ ks show at most a weak dependence on energy during the three *Chandra* observations, while the *XMM-Newton* observation exhibits significantly softer variability. An examination of the relationship between the 0.4–3.4 keV and 3.4–8.0 keV intensities revealed erratic, short-term (timescale ~ 1000 s) spectral variations during visit 1, which are seen as deviations from the mean relation between the soft-band and hard-band intensities. During visit 2, the relationship between the 0.4–2.7 keV and 4.2–8.0 keV intensities was flatter than in the other observations (Fig. 5). During observation 882 the object reached higher intensities compared to visit 1 and visit 2.

Simultaneous UV observations were conducted during part of the second *Chandra* observation. We detected a zero-lag correlation between the X-ray and UV fluxes with a significance of ~ 99.5 %. The upper limit on any lag between the two light curves is roughly ± 1 hour.

5.2. X-ray Variability

5.2.1. Comparison with the *XMM-Newton* Observation

The 2–10 keV fluxes during visit 1, visit 2 and observation 882 were $\sim 2.5 \times 10^{-12}$, $\sim 3.0 \times 10^{-12}$ and $\sim 3.5 \times 10^{-12}$ erg cm $^{-2}$ s $^{-1}$, respectively. In comparison, the 2–10 keV flux during the *XMM-Newton* observation was $\sim 5.5 \times 10^{-12}$ erg cm $^{-2}$ s $^{-1}$. Our variability analysis suggests, then, that the short-term ($\lesssim 15$ ks) variability is significantly softer when the overall flux level is higher.

In Fig. 10 we show the relationship between the 0.4–3.4 keV and 3.4–8.0 keV counting rates during the *XMM-Newton* observation, with a time resolution of 1000 s. While a detailed analysis of the *XMM-Newton* data is beyond the scope of this paper, Fig. 10 shows clearly that the softness increases as the flux increases. During the *Chandra* observations, NGC 4395 occupied only the lower part of this track (i.e., below the dashed line), with no excursions to the upper, softer region (i.e., above the dashed line). (There is, however, a hint in Fig. 5 that, during observation 882, the source softness increased at the time of highest soft-band counting rate.) NGC 4395 exhibited stronger flares during the *XMM-Newton* observation than during the *Chandra* observations. Consequently, the *XMM-Newton* data exhibit both higher flux and softer variability.

5.2.2. Long-Term Spectral Variability

The simplest model for explaining the X-ray variability is to suppose that variations in a single parameter, such as mass-accretion rate, produces variability on both short and long timescales. As this parameter varies, the object will trace out a track in a plot of soft-band versus hard-band intensity. Different overall flux levels, and spectral properties, then correspond to different locations along this track. During visit 2, however, a different track is traced out compared to visit 1 and observation 882. This shows that the long-term (i.e., *inter*-observation, $\gtrsim 30$ ks) variability between these two observations is in a different sense from the short-term (i.e. *intra*-observation, $\lesssim 30$ ks) variability. Between visit 1 and visit 2 the mean hard-band (3.4–8.0 keV) counting rate does not change significantly while the soft-band (0.4–3.4 keV) counting rate is scaled down.

One possibility for this spectral change is that the underlying power law may have flattened between visit 1 and visit 2. In the two-phase model of AGNs (and also black hole binary) X-ray emission, the hot phase (i.e., the corona) inverse-Compton scatters seed photons from the cold phase (i.e., the disk) (Shapiro et al. 1976; Sunyaev & Titarchuk 1980; Haardt & Maraschi 1991, 1993). The corona and disk are radiatively coupled so that some fraction of the photons scattered in the corona return to the disk and are reprocessed to become seed photons, which for AGNs are seen presumably at UV wavelengths. In this scenario, the photon index of the power-law emission depends on the rate at which energy is dissipated into the corona, the physical properties of the corona, and the geometry of the disk-corona system.

For a pair-dominated corona, variations in the compactness can produce variations in the photon index (e.g., Stern et al. 1995; Haardt et al. 1997). In this case, a decrease in the luminosity will be associated with a flattening of the spectrum. This effect is unlikely to explain a decrease in the photon index between the visit 1 and visit 2 *Chandra* observations because we observed no significant change in the hard-band counting rate. The compactness can vary also if the size of the emission region varies. A flattening of the spectrum, without a change in the source flux, could be caused by an increase in the size of the corona. Alternatively, for a corona not dominated by pairs, a variation in optical depth can, in principle, produce a change in the photon index of the spectrum without an associated variation in the observed flux (Haardt et al. 1997).

Variations in the photon index can also be caused by a changes in the accretion geometry, as this will influence the amount by which the corona is “starved” of photons (e.g., Haardt et al. 1994; Stern et al. 1995; Zdziarski et al. 1998). For example, a patchy corona can produce relatively hard spectra because a reduction in the coronal covering fraction will reduce the seed flux that enters the corona. Similarly, a centrally located spherical corona

may be photon starved. Variations in geometry have been proposed to explain the spectral variability associated with state changes in galactic black hole binaries (Esin et al. 1997; Zdziarski 1998). These seem highly unlikely in the case of NGC 4395, however, given the lack of hard flux variability and the short timescale of the variations, which correspond only to a few seconds in a galactic binary. State changes are usually seen on much longer time scales (a few days), although an exception to this is the microquasar GRS 1915+105. In this object, unusual “state” changes are observed on a timescale of seconds (Belloni et al. 1997a,b), but are accompanied by large changes in flux, so cannot apply in NGC 4395.

The fundamental problem with intrinsic continuum changes is that to get a large change in spectral index without any change in the hard-band counting rate requires a high degree of fine tuning. Any pivoting of the spectrum would need to be counteracted exactly by an appropriate variation in the flux normalization, which would depend on the pivot energy. Given this, arguably a more likely explanation for the scaling down of the soft-band intensity between visit 1 and visit 2 is an increase in absorption. Iwasawa et al. (2000) and Shih et al. (2003) have already shown evidence of a multi-zone ionized absorber in this object, and attributed short-term spectral changes to variations of the ionization parameter in response to the continuum flux. We can rule out this interpretation for the inter-observation spectral variability between visits 1 and 2 because the mean hard-band intensity does not change between the observations. Rather, there would need to be an increase in the column density of the absorber, or a change in ionization unrelated to the continuum. Recent detailed modeling of UV and X-ray absorbers of some sources have shown clear evidence for variations of absorbing gas due to transverse motion of gas through the line of sight (e.g., Gabel et al. 2003; Kraemer et al. 2005), and this appears to be the most likely mechanism to account for the variations in NGC 4395.

5.2.3. Short-Term Spectral Variability

Significant scatter about the mean relation between the counting rates in two bands has been seen previously in Seyfert galaxies (see, e.g., the “flux-flux plots” of Taylor et al 2003). NGC 4395 exhibited erratic spectral variations during visit 1, and these were seen as deviations from the mean relation between the 0.4–3.4 and 3.4–8.0 keV counting rates. Unfortunately, our data do not have a high-enough signal-to-noise ratio to investigate the nature of these variations in detail. We consider below possible explanations for how the spectral variations might be produced either within, or outside of, the X-ray emission region.

One explanation was mentioned by Moran et al. (2005) in the context of observation 882. Those authors found significant variations in the ratio between the counting rates in 0.3–

1.2 keV and 2–10 keV (i.e., different from our “soft” and “hard” bands), and they suggested that these variations are produced by changes in the column density of a single-zone warm absorber. In this kind of scenario, the erratic variations are superimposed on the existing short-term variability.

An alternative possibility is that the *underlying* variability in the various energy bands becomes uncorrelated at times. At the most basic level, the loss of coherence between the soft and hard intensities rules out the simplest, single-temperature Comptonization models. In these models, any spectral variations should be smooth (e.g., Haardt et al. 1997).

The presence of scatter about the mean relation between the soft-band and hard-band counting rates is possibly a manifestation of a hardening of the power spectrum at high frequencies, as is seen, for example, in NGC 7469 (Nandra & Papadakis 2001) and MCG–6-30-15 (Vaughan et al. 2003b; Vaughan & Fabian 2004; Papadakis et al. 2005). In the context of “propagating perturbation” models (Lyubarskii 1997; Churazov et al. 2001; Kotov et al. 2001), variations in the mass accretion rate are injected into the accretion flow over a wide range of disk radii, with the timescale of the variations being longer for larger radii. These perturbations then propagate inward and give rise to f^{-1} variations in the accretion rate at the emission region. The variations at frequencies greater than the power-spectral break are assumed to originate from within the emission region itself. The inner parts of this region experience faster perturbations, and produce harder spectra, than the outer parts, thus causing the power spectrum above the break frequency to flatten with increasing energy. In NGC 4395, this power-spectral break is at a timescale of ~ 500 s (Vaughan et al. 2004, see § 1). Our correlation analysis, however, does not probe these short timescales, so we cannot appeal to propagating perturbations to explain the observed lack of coherence.

One alternative is to invoke a shot-type model (e.g., Terrell 1972) in which there are many short-lived, disconnected emitting regions, or ‘flares’. If these regions possess differing spectral properties, then the spectral shape of their combined X-ray emission might be expected to vary. Note, however, that shot-noise models are challenged by the combined presence of a linear rms-flux correlation and a log-normal distribution of fluxes (Uttley & McHardy 2001; Uttley 2004; Uttley et al. 2005).

5.3. X-ray–UV Connection

The two-phase model (Haardt & Maraschi 1991) predicts that the X-ray and UV emission should be linked (see also Guilbert & Rees 1988). The number of objects in which a definite link has been observed is somewhat controversial (see Maoz et al. 2002, and refer-

ences therein). The best examples thus far are NGC 5548 (Clavel et al. 1992), NGC 4151 (Edelson et al. 1996), and NGC 7469 (Nandra et al. 2000; Petrucci et al. 2004). In the last object, a correlation was seen between the UV flux and X-ray photon index, rather than between the UV and X-ray fluxes. In a number of other objects there is a very poor correlation between the bands, particularly on short time scales (e.g., Done et al. 1990; Edelson et al. 2000).

The zero-lag correlation between the X-ray and UV fluxes during visit 2 has a detection significance of $\sim 99.5\%$. This is a conservative estimate as it accounts for the possibility of the chance alignment of two independent flicker-noise light curves. NGC 4395 thus satisfies a basic prediction of two-phase models. The X-ray flux illuminates the material responsible for the (pseudo-thermal) UV emission (e.g., the accretion disk), which in turn reprocesses them into UV seed photons to be Compton upscattered into the X-ray band.

The two-phase model predicts that the luminosity of the reprocessed component should have the same order of magnitude as the X-ray luminosity (Haardt et al. 1994). This implies that the amplitude of the UV flux variability should be roughly the same as that of the X-rays. We determined the fluxes of the variable X-ray and UV components by measuring the square-root of the *unnormalized* excess variance of the X-ray and UV data that were collected exactly simultaneously. The monochromatic flux variability was $\sim 2 \times 10^{-13} \text{ erg cm}^{-2} \text{ s}^{-1}$ at both 1350 Å and 1 keV. We must stress that the comparison we perform here is very uncertain; a rigorous analysis would require broad-band luminosity measurements. This is, unfortunately, hampered by the difficulties in modeling the ionized absorber in the X-ray spectrum and the fact that useful data cannot be obtained in the extreme UV band. Nevertheless, the fact that the X-ray and UV flux variabilities have the same order of magnitude suggests that an interpretation within the two-phase model framework is energetically reasonable.

The relationship between the X-ray and UV fluxes shown in Fig. 9 suggests that the UV flux contains a non-reprocessed component of $\sim 7 \times 10^{-16} \text{ erg cm}^{-2} \text{ s}^{-1} \text{ Å}^{-1}$, which is roughly 65 % of the mean flux. In the context of the two-phase model, this flux may be attributed to intrinsic emission from the accretion disk. In this scenario, only a portion of the accretion power is dissipated in the corona, which itself must be patchy (Haardt et al. 1994, 1997).

From a cross-correlation analysis, the upper limit on the time lag between the X-ray and UV fluxes is about ± 1 hour. The distance between the reprocessor and the corona must, therefore, be separated by a distance not greater than $\sim 10^{14}$ cm. For a black hole mass of $M_{\bullet} = (3.6 \pm 0.6) \times 10^5 M_{\odot}$, this corresponds to a distance of about 2000 r_g ($r_g = GM_{\bullet}/c^2$). The upper limit on the time lag we measured is consistent with the measured lag between the UV continuum and line fluxes found by Peterson et al. (2005).

It is worth noting here that Skelton et al. (2005, see also Desroches et al. 2006) observed $\sim 10\%$ variations in the optical continuum of NGC 4395, over timescales of roughly 30 minutes to 8 hours. They pointed out that this optical variability is much more rapid than expected if the variability is the result of instabilities in the disk. The rapid variations are, however, quite naturally explained in the context of X-ray reprocessing. The current puzzle is why this mechanism appears to operate in some sources, including NGC 4395, but not in others. A possible solution can be seen in the complex behavior we see in NGC 4395, which suggests several different origins for the flux and spectral variability (e.g. in the seed photons, intrinsic to corona, associated with absorption). Clearly the presence or absence of any UV/X-ray correlation will depend on the dominant mode of variability at the time of a given observation.

5.4. A Real Periodicity at 341 s?

While many claims have been made, no periodic or quasi-periodic signal has yet been robustly detected in an AGN (see Vaughan 2005). The detection significance of 99.0 % that we calculated for the feature at 341 s in the visit 1 power spectrum represents one of the best candidate signals found thus far. A feature at 390 s was present also during the second half of observation 882, with a detection significance of 95.0 %, in agreement with the analysis of Moran et al. (2005).

This power-spectral feature, however, should be interpreted very cautiously. First, it was not detected during either visit 2 or the *XMM-Newton* observation. Having searched for the feature in these data, the overall “number-of-trials” is thus more than just the number of independent frequencies in the visit 1 power spectrum. Second, excess power was found only in a single frequency bin, which would correspond to a quality factor ($Q = \nu/FWHM$) of greater than about 90. In contrast, the *quasi*-periodic oscillations seen in galactic black hole binaries are broader than this, with quality factors of up to only about 30 (Remillard et al. 2002). Given that the broad-band variability is similar in AGNs and black hole binaries, we might also expect similarities with regard to quasi-periodic oscillations. A genuine detection cannot yet be claimed, although NGC 4395 remains a promising candidate for future studies.

We thank Harvey Tananbaum, the Chandra X-ray Center Director, for awarding Director’s Discretionary Time. We thank also the anonymous referee for constructive comments that improved the manuscript. PMO acknowledges financial support from PPARC. AL acknowledges support by the Israel Science Foundation (Grant #1030/04), and by a grant from the Norman and Helen Asher Space Research Institute. SK is supported in part at

the Technion by a Zeff Fellowship. This research is supported by NASA through *HST* grant GO-09818 from the Space Telescope Science Institute, which is operated by the Association of Universities for Research in Astronomy, Inc., under NASA Contract NAS5-26555. A.V.F. is also grateful for the assistance of National Science Foundation (NSF) grant AST-0307894. L.-B.D. is supported by a Julie-Payette/Doctoral Fellowship from the Natural Sciences and Engineering Research Council of Canada and by the Canadian Space Agency.

REFERENCES

- Alexander, T. 1997, in *Astronomical Time Series*, ed. D. Maoz, A. Sternberg, & E. M. Leibowitz (Dordrecht: Kluwer), 163
- Belloni, T., Mendez, M., King, A. R., van der Klis, M., & van Paradijs, J. 1997a, *ApJ*, 488, L109
- . 1997b, *ApJ*, 479, L145
- Churazov, E., Gilfanov, M., & Revnivtsev, M. 2001, *MNRAS*, 321, 759
- Clavel, J., et al. 1992, *ApJ*, 393, 113
- Desroches, L., et al. 2006, *ApJ*, submitted
- Done, C., Ward, M. J., Fabian, A. C., Kunieda, H., Tsuruta, S., Lawrence, A., Smith, M. G., & Wamsteker, W. 1990, *MNRAS*, 243, 713
- Edelson, R. A., & Krolik, J. H. 1988, *ApJ*, 333, 646
- Edelson, R. A., et al. 1996, *ApJ*, 470, 364
- Edelson, R., et al. 2000, *ApJ*, 534, 180
- Esin, A. A., McClintock, J., & Narayan, R. 1997, *ApJ*, 489, 865
- Filippenko, A. V., & Ho, L. C. 2003, *ApJ*, 588, L13
- Filippenko, A. V., Ho, L. C., & Sargent, W. L. W. 1993, *ApJ*, 410, L75
- Filippenko, A. V., & Sargent, W. L. W. 1989, *ApJ*, 342, L11
- Gabel, J. R., et al. 2003, *ApJ*, 595, 120
- Gaskell, C. M., & Sparke, L. S. 1986, *ApJ*, 305, 175

- Guilbert, P. W., & Rees, M. J. 1988, MNRAS, 233, 475
- Haardt, F., & Maraschi, L. 1991, ApJ, 380, L51
- . 1993, ApJ, 413, 507
- Haardt, F., Maraschi, L., & Ghisellini, G. 1994, ApJ, 432, L95
- Haardt, F., Maraschi, L., & Ghisellini, G. 1997, ApJ, 476, 620
- Iwasawa, K., Fabian, A. C., Almaini, O., Lira, P., Lawrence, A., Hayashida, K., & Inoue, H. 2000, MNRAS, 318, 879
- Kotov, O., Churazov, E., & Gilfanov, M. 2001, MNRAS, 327, 799
- Kraemer, S. B., et al. 2005, ApJ, 633, 693
- Lyubarskii, Y. E. 1997, MNRAS, 292, 679
- Maoz, D., Markowitz, A., Edelson, R., & Nandra, K. 2002, ApJ, 124, 1988
- Maoz, D., & Netzer, H. 1989, MNRAS, 236, 21
- Moran, E. C., Eracleous, M., Leighly, K. M., Chartas, G., Filippenko, A. V., Ho, L. C., & Blanco, P. R. 2005, AJ, 129, 2108
- Nandra, K., Le, T., George, I. M., Edelson, R. A., Mushotzky, R. F., Peterson, B. M., & Turner, T. J. 2000, ApJ, 544, 734
- Nandra, K., & Papadakis, I. 2001, ApJ, 554, 710
- Papadakis, I. E., Kazanas, D., & Akylas, A. 2005, ApJ, 631, 727
- Papadakis, I. E., & Lawrence, A. 1993, MNRAS, 261, 612
- Peterson, B. M., Wanders, I., Horne, K., Collier, S., Alexander, T., Kaspi, S., & Maoz, D. 1998, PASP, 110, 660
- Peterson, B. M., et al. 2004, ApJ, 613, 682
- Peterson, B. M., et al. 2005, ApJ, 632, 799
- Petrucci, P. O., Maraschi, L., Haardt, F., & Nandra, K. 2004, A&A, 413, 477

- Press, W. H., Teukolsky, S. A., Vetterling, W. T., & Flannery, B. P. 2001, *Numerical Recipes in Fortran 77: The Art of Scientific Computing* (Cambridge: Cambridge University Press)
- Remillard, R., Muno, M., McClintock, J., & Orosz, J. 2002, in *New Views on Microquasars*, ed. P. Durouchoux, Y. Fuchs, & J. Rodriguez (Kolkata (India): Centre for Space Physics), 49
- Shapiro, S. L., Lightman, A. P., & Eardley, D. M. 1976, *ApJ*, 204, 187
- Shih, D. C., Iwasawa, K., & Fabian, A. C. 2003, *MNRAS*, 341, 973
- Skelton, J. E., Lawrence, A., Pappa, A., Lira, P., & Almaini, O. 2005, *MNRAS*, 358, 781
- Stern, B. E., Poutanen, J., Svensson, R., Sikora, M., & Begelman, M. C. 1995, *ApJ*, 449, L13
- Sunyaev, R., & Titarchuk, L. G. 1980, *A&A*, 86, 121
- Taylor, R. D., Uttley, P., & McHardy, I. M. 2003, *MNRAS*, 342, L31
- Terrell, N. J. J. 1972, *ApJ*, 174, L35
- Timmer, J., & Konig, M. 1995, *A&A*, 300, 707
- Uttley, P. 2004, *MNRAS*, 347, L61
- Uttley, P. & McHardy, I. M. 2001, *MNRAS*, 323, L26
- Uttley, P., McHardy, I. M., & Vaughan, S. 2005, *MNRAS*, 359, 345
- Vaughan, S. 2005, *A&A*, 391, 391
- Vaughan, S., Edelson, R., Warwick, R. S., & Uttley, P. 2003a, *MNRAS*, 345, 1271
- Vaughan, S., & Fabian, A. C. 2004, *MNRAS*, 348, 1415
- Vaughan, S., Fabian, A. C., & Nandra, K. 2003b, *MNRAS*, 339, 1237
- Vaughan, S., Iwasawa, K., Fabian, A. C., & Hayashida, K. 2004, *MNRAS*, 356, 524
- White, R. J., & Peterson, B. M. 1994, *PASP*, 106, 879
- Zdziarski, A. A. 1998, *MNRAS*, 296, L51

Zdziarski, A. A., Poutanen, J., Mikolajewska, J., Gierlinski, M., Ebisawa, K., & Johnson, W. N. 1998, MNRAS, 301, 435

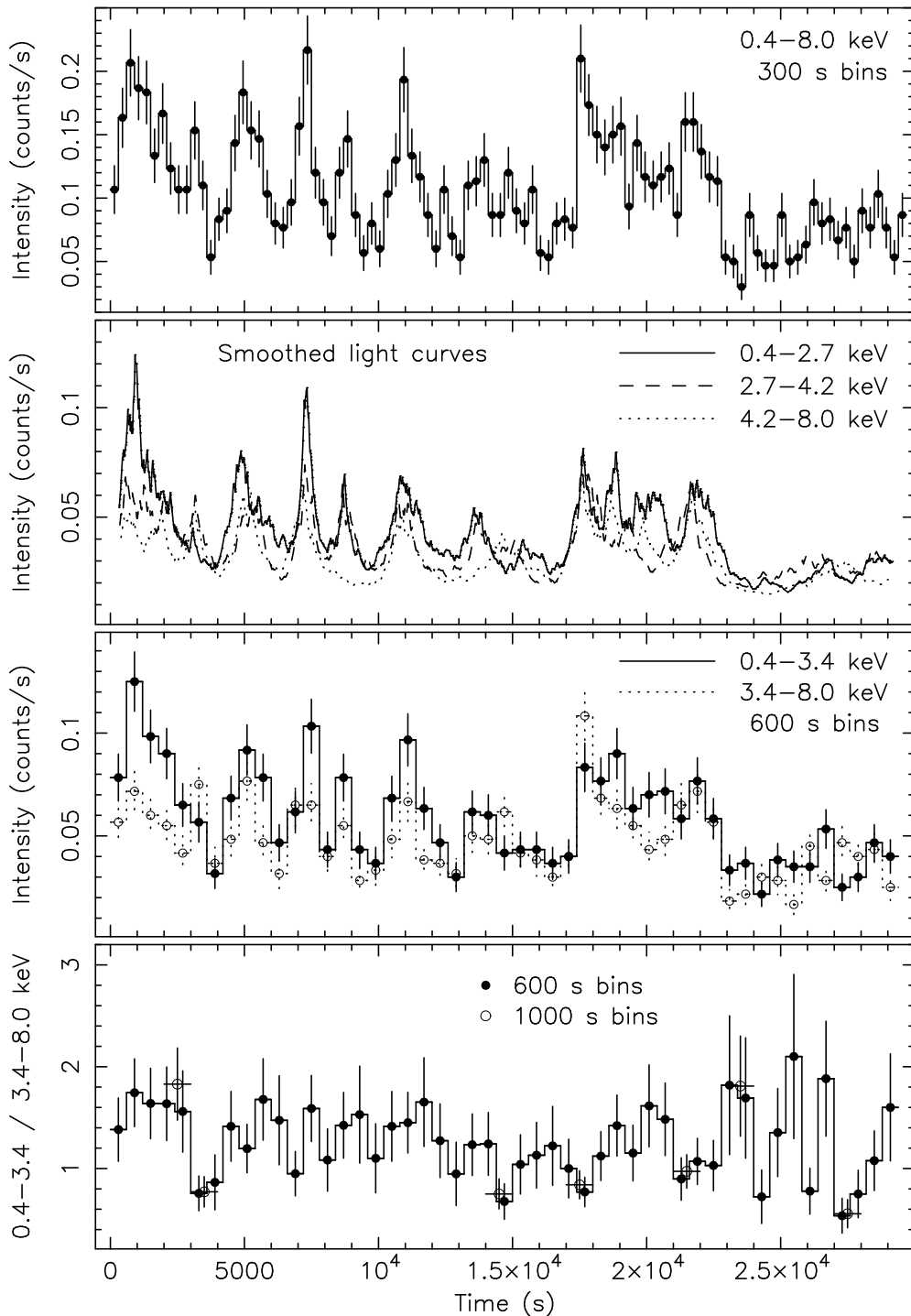


Fig. 1.— Full-band (0.4–8.0 keV) and energy-resolved light curves for visit 1. The smoothed light curves show the running means calculated from overlapping groups of 30 consecutive events. In the bottom panel, the solid circles show the softness calculated from 600 s bins, and the open circles correspond to 1000 s bins. These open circles are shown for the seven points that each contribute $\Delta\chi^2 > 2$ to the straight-line fit between the soft and hard intensities shown in Fig. 5.

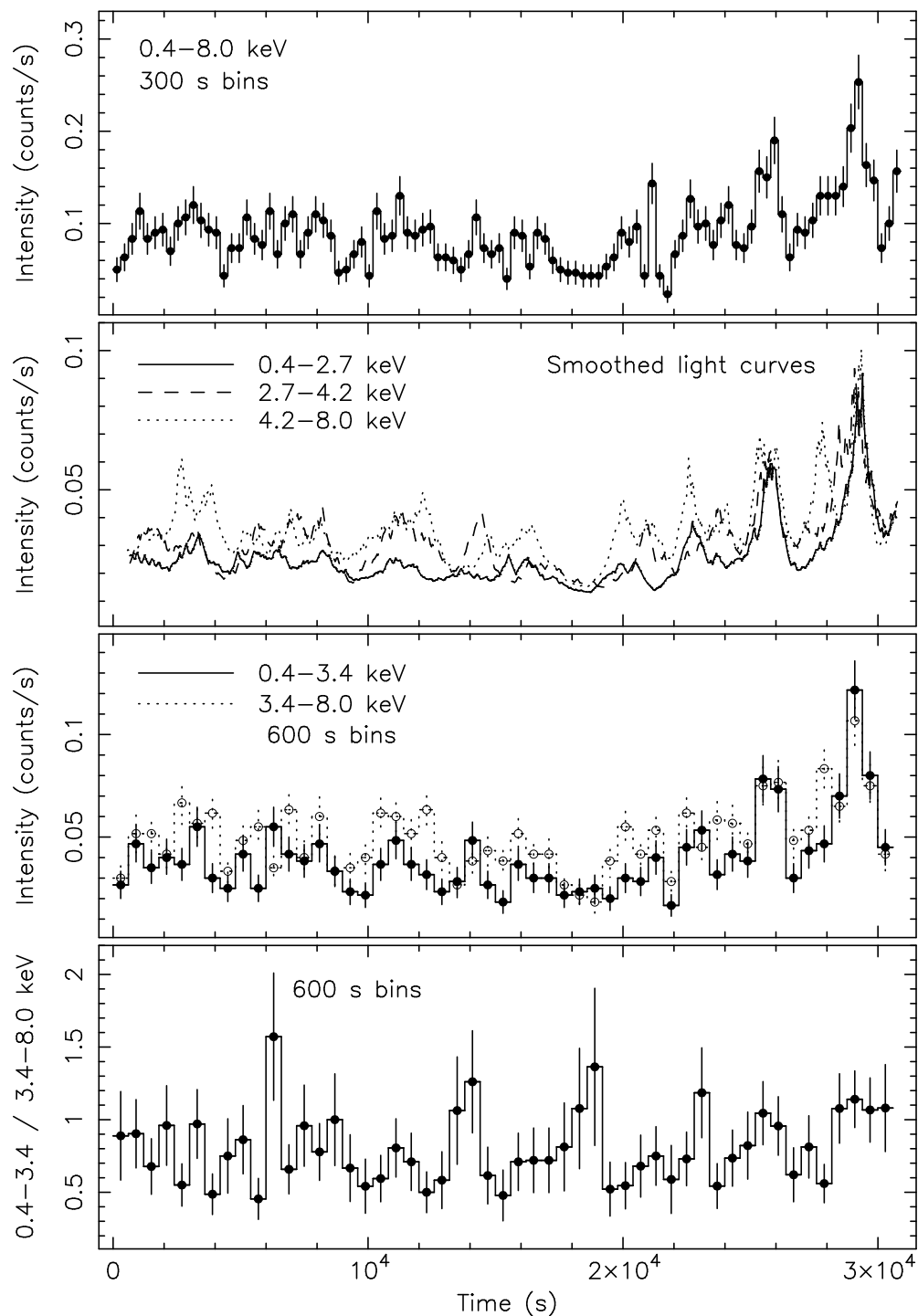


Fig. 2.— Full-band (0.4–8.0 keV) and energy-resolved light curves for visit 2. The smoothed light curves show the running means calculated from overlapping groups of 30 consecutive events.

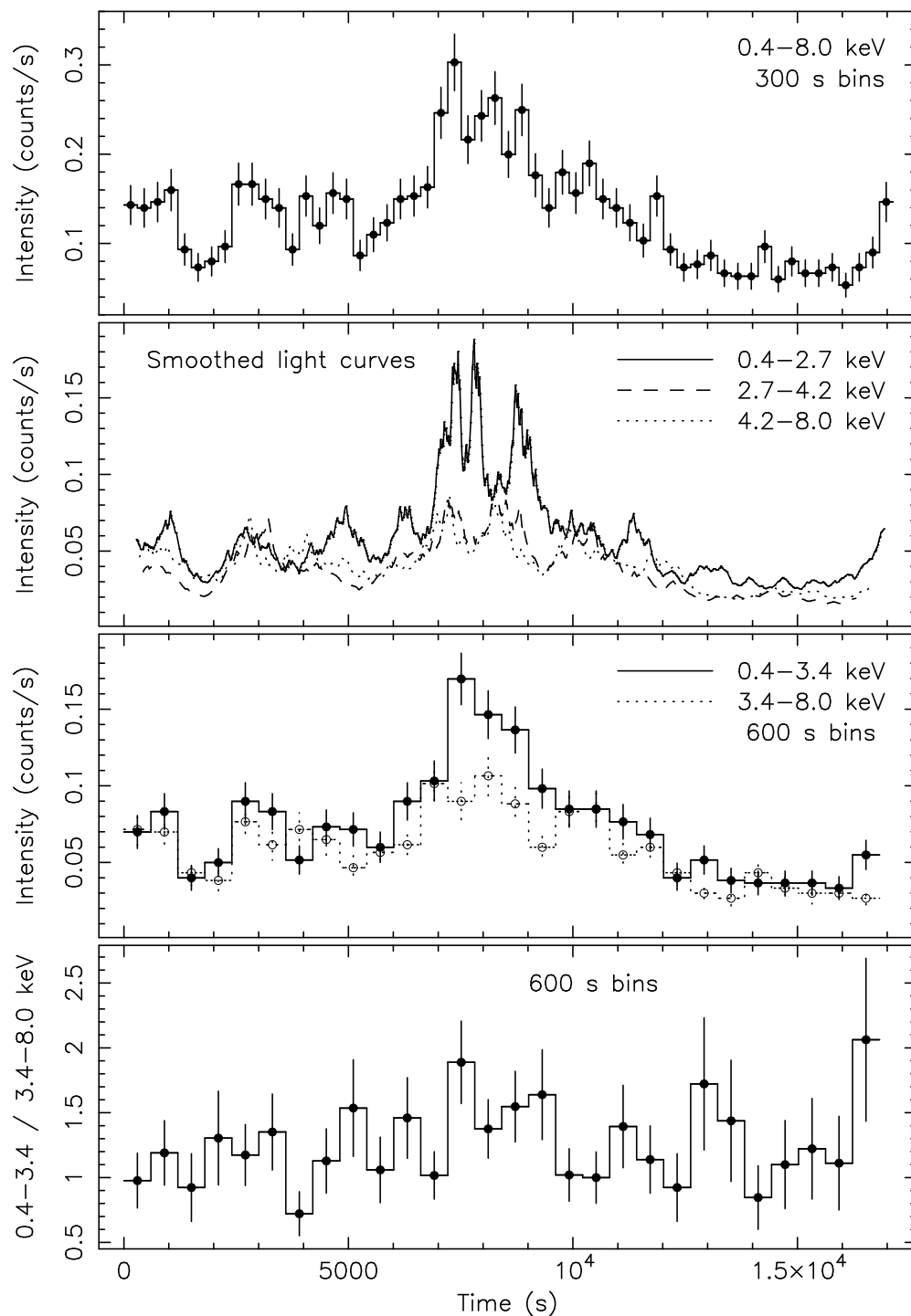


Fig. 3.— Full-band (0.4–8.0 keV) and energy-resolved light curves for observation 882. The smoothed light curves show the running means calculated from overlapping groups of 30 consecutive events.

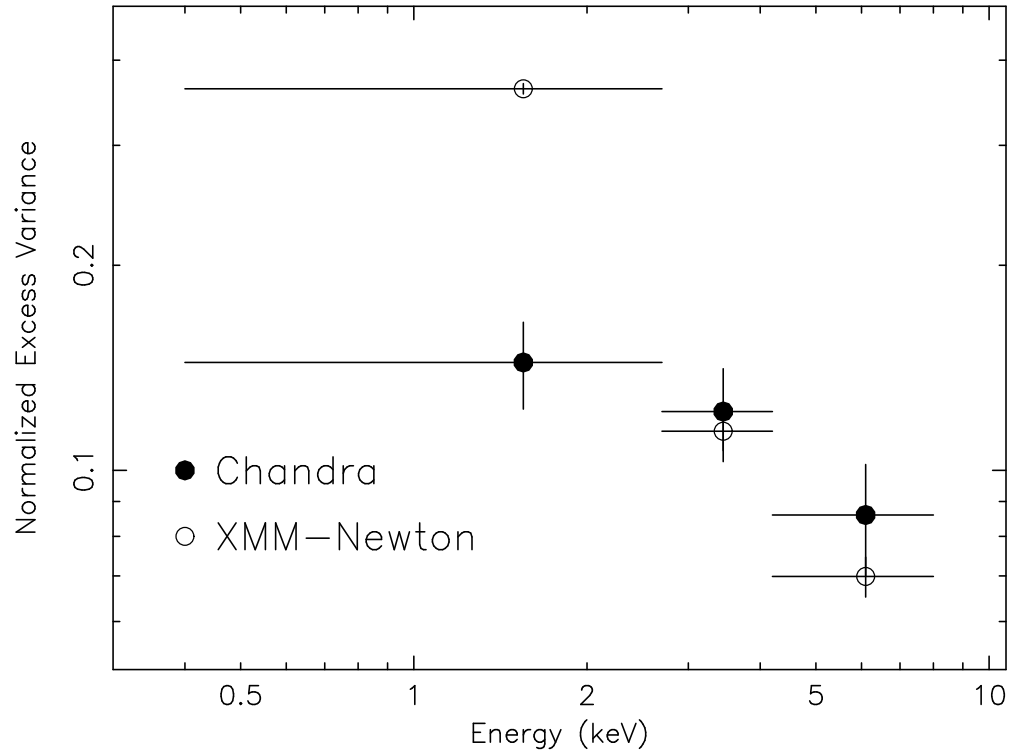


Fig. 4.— Normalized excess variances in the energy bands 0.4–2.7–4.2–8.0 keV, for 600–15000 s timescales. The filled circles show the mean variance of the *Chandra* observations while the open circles correspond to the *XMM-Newton* data. The error bars show the uncertainties expected from Poisson noise only.

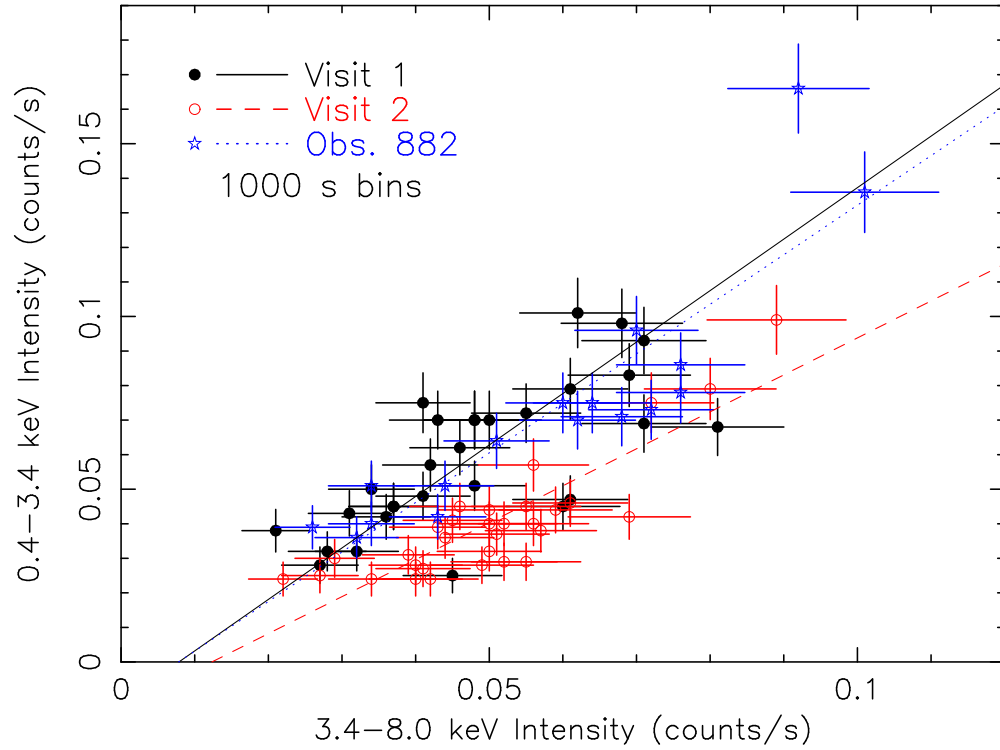


Fig. 5.— Correlations between the 0.4–3.4 keV and 3.4–8.0 keV intensities during visit 1 (solid circles, black in electronic edition), visit 2 (open circles, red in electronic edition) and *Chandra* observation 882 (stars, blue in electronic edition). Each datum corresponds to a time bin of 1000 s. The best-fitting straight lines for visit 1, visit 2, and observation 882 are shown as solid (black in electronic edition), dashed (red in electronic edition), and dotted (blue in electronic edition) lines, respectively. See the electronic edition of the Journal for a color version of this figure.

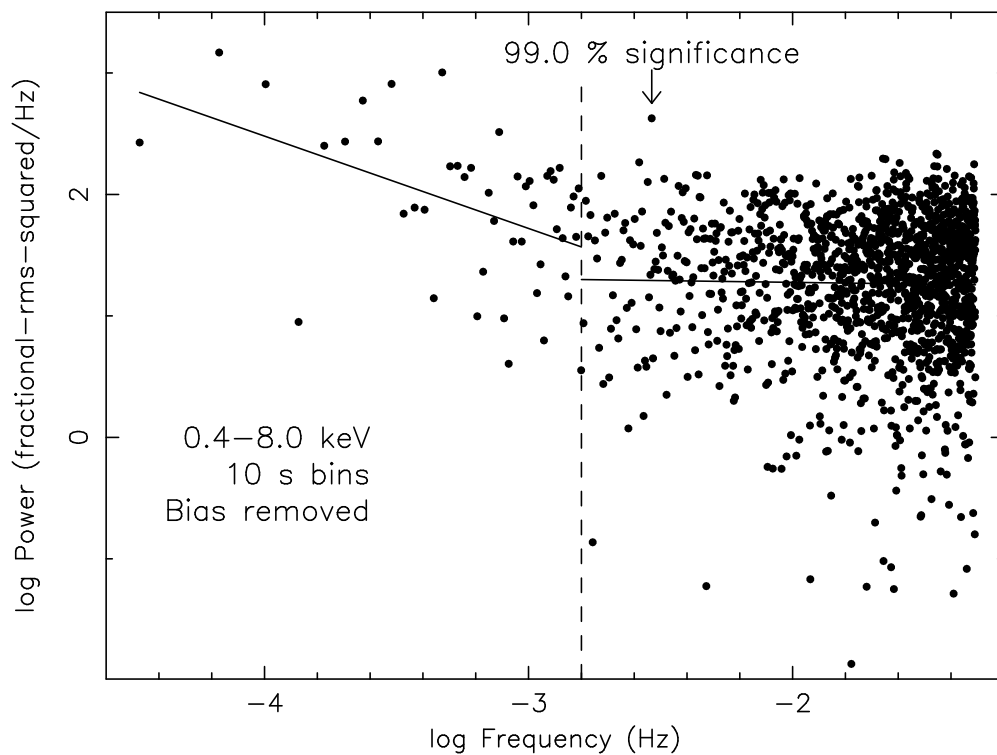


Fig. 6.— Full-band (0.4–8.0 keV) power spectrum from visit 1, using a time resolution of 10.14392 s. The logarithm (base 10) of the power is plotted versus the logarithm of frequency, and the constant bias has been removed (see text). The solid lines show the least-squares linear models for frequencies below $10^{-2.8}$ Hz (indicated with the dashed line) and above $10^{-2.8}$ Hz. The most significant power above the continuum is at a frequency of 2.93×10^{-3} Hz, and is indicated with the arrow.

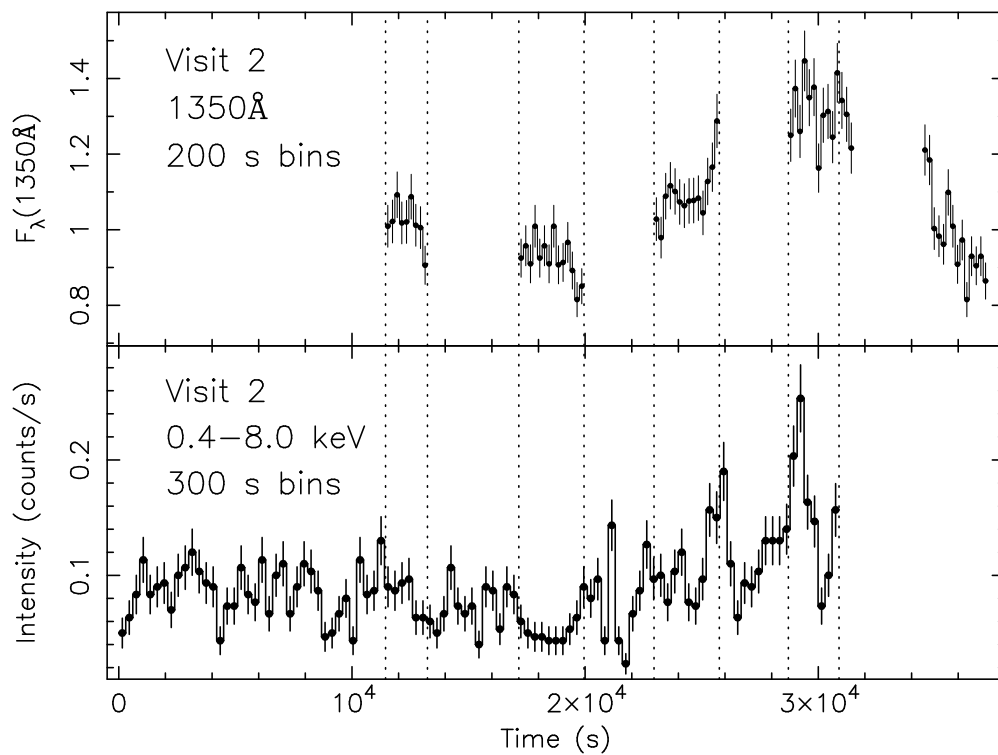


Fig. 7.— UV continuum flux density at 1350 Å (top) and full-band (0.4–8.0 keV) intensity (bottom) during visit 2. The UV and X-ray light curves use time resolutions of 200 s and 300 s, respectively. The UV data are from Peterson et al. (2005) and the flux is in units of $10^{-15} \text{ erg cm}^{-2} \text{ s}^{-1} \text{ \AA}^{-1}$. The dotted lines indicate the boundaries of the time intervals having simultaneous X-ray and UV observations.

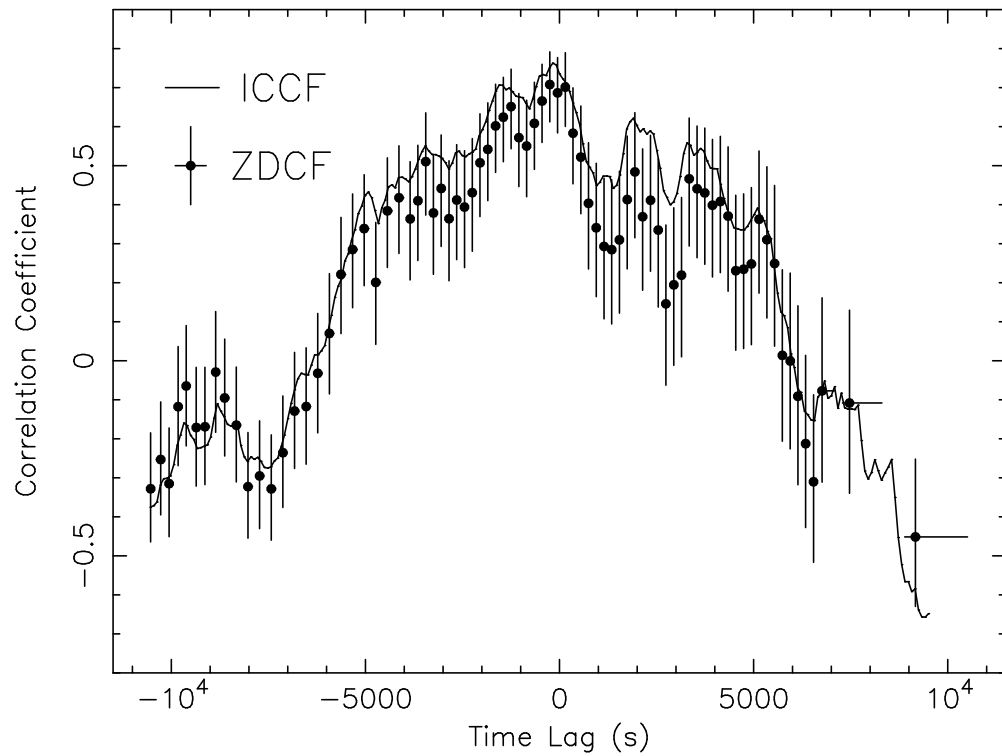


Fig. 8.— Cross-correlation function between the UV continuum flux density at 1350 \AA and the $0.4\text{--}8.0 \text{ keV}$ intensity. The solid line and solid symbols correspond, respectively, to the ICCF and ZDCF methods.

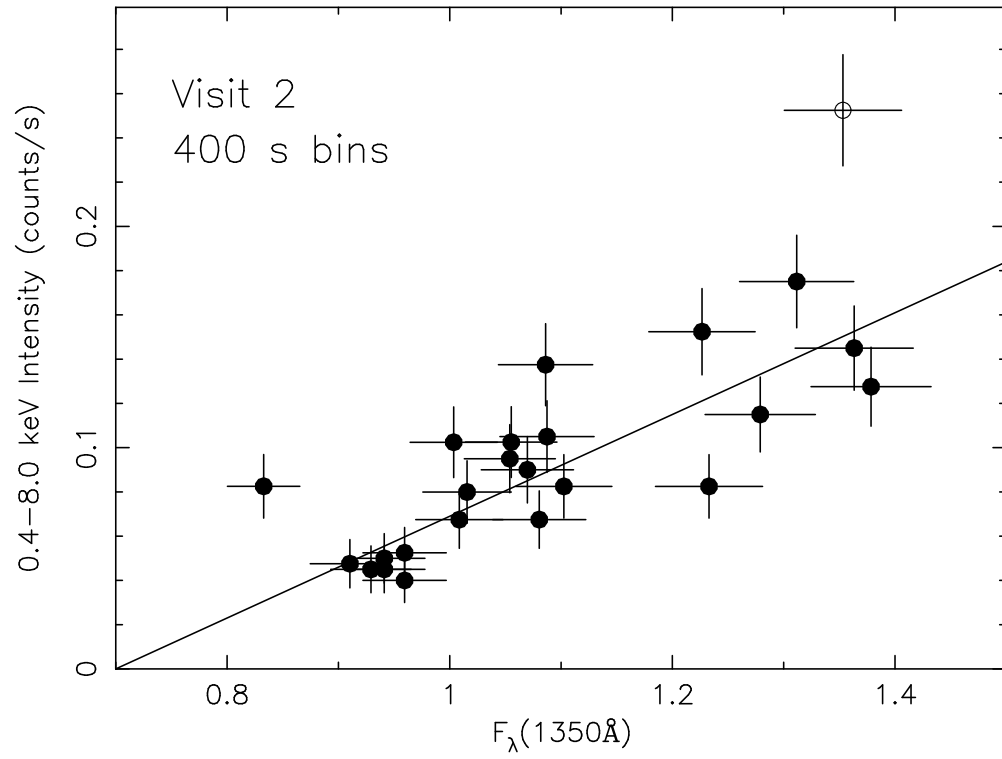


Fig. 9.— Full-band (0.4–8.0 keV) intensity versus the UV flux at 1350 Å during visit 2, using simultaneous 400 s time bins. The UV flux in both panels is in units of 10^{-15} erg cm^{-2} s^{-1} Å $^{-1}$. The line shows the best-fitting linear model, which intercepts the horizontal axis at ~ 0.7 . The datum indicated with an open symbol was not included in the linear fit.

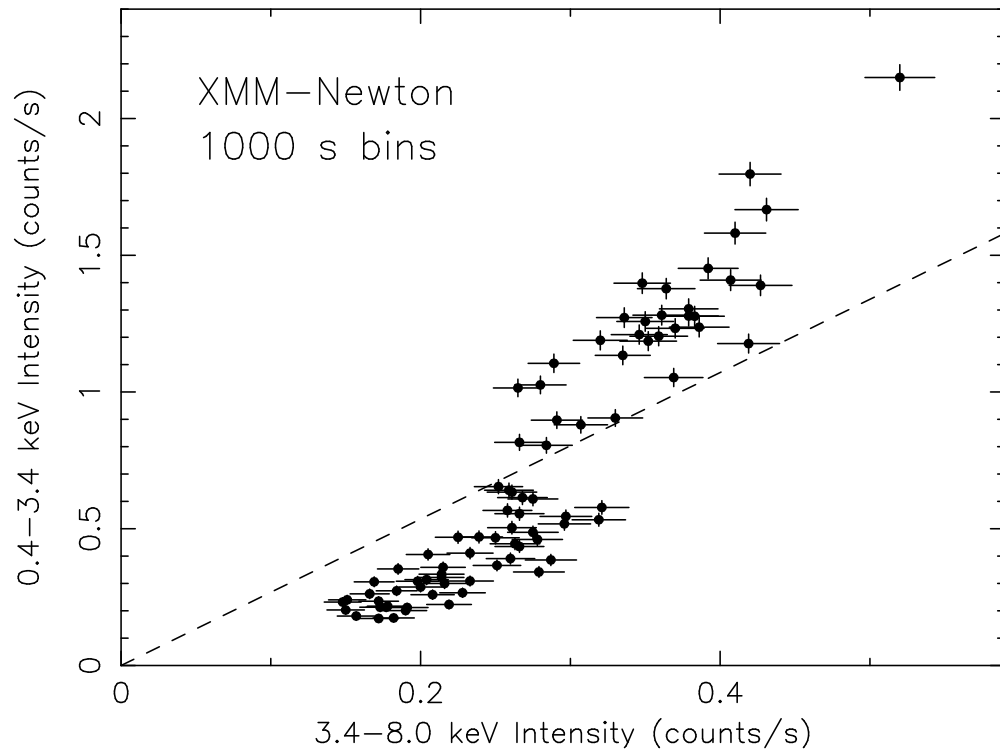


Fig. 10.— Correlation between the 0.4–3.4 keV and 3.4–8.0 keV intensities during the *XMM-Newton* observation showing the softening of the spectrum with increasing flux. Each datum corresponds to a time bin of 1000 s. The *Chandra* observations occupy roughly the region below the dashed line.

Table 1. Normalized excess variance measurements.

Energy Range (keV)	Normalized Excess Variance ($\times 10^{-2}$)				
	Visit 1	Visit 2	Obs. 882	<i>Chandra</i>	<i>XMM-Newton</i>
0.4–8.0	10.7 ± 1.4	10.6 ± 1.6	16.2 ± 1.9	11.8 ± 0.9	23.7 ± 0.4
0.4–3.4	11.0 ± 2.0	15.5 ± 3.3	19.9 ± 3.1	14.5 ± 1.7	33.0 ± 0.6
3.4–8.0	10.9 ± 2.4	7.4 ± 1.9	12.6 ± 2.6	9.8 ± 1.3	7.9 ± 0.4
0.4–2.7	13.5 ± 2.8	11.8 ± 3.9	21.5 ± 4.0	14.4 ± 2.1	36.3 ± 0.6
2.7–4.2	9.4 ± 2.7	11.3 ± 3.2	19.7 ± 4.3	12.2 ± 1.9	11.4 ± 0.7
4.2–8.0	9.1 ± 2.9	7.9 ± 2.5	8.8 ± 3.0	8.6 ± 1.6	7.0 ± 0.5

Note. — Light-curve duration 15 ks, time resolution 600 s.